

Influence of the triangular Mn-O breathing mode on the magnetic ordering in multiferroic hexagonal manganites

Tara N. Tošić,^{1,*} Quintin N. Meier,^{2,1} and Nicola A. Spaldin¹

¹*Materials Theory, ETH Zurich, Wolfgang-Pauli-Strasse 27, 8093 Zürich, Switzerland*

²*Université Grenoble Alpes, CEA, LITEN, 17 rue des Martyrs, 38054 Grenoble, France*

(Dated: February 7, 2022)

We use a combination of symmetry analysis, phenomenological modelling and first-principles density functional theory to explore the interplay between the magnetic ground state and the detailed atomic structure in the hexagonal rare-earth manganites. We find that the magnetic ordering is sensitive to a breathing mode distortion of the Mn and O ions in the ab plane, which is described by the K_1 mode of the high-symmetry structure. Our density functional calculations of the magnetic interactions indicate that this mode particularly affects the single-ion anisotropy and the inter-planar symmetric exchanges. By extracting the parameters of a magnetic model Hamiltonian from our first-principles results, we develop a phase diagram to describe the magnetic structure as a function of the anisotropy and exchange interactions. This in turn allows us to explain the dependence of the magnetic ground state on the identity of the rare-earth ion and on the K_1 mode.

I. INTRODUCTION

The hexagonal manganites, h - $RMnO_3$, where $R =$ In, Sc, Y, and Dy to Lu, are a class of multiferroic materials that show a combination of improper ferroelectricity and antiferromagnetism. Their hexagonal symmetry results in almost degenerate free energy surfaces in the hexagonal ab plane for both the improper ferroelectric distortion [1–4] and for the magnetic order [1, 5, 6]. As a consequence of these quasi-degenerate ferroelectric and magnetic energy surfaces, small changes in the crystal chemistry lead to different structural and magnetic ground states. For example, in $InMnO_3$, small variations in the defect concentration favour either the improper ferroelectric state or a related antipolar phase [7, 8]. The magnetic energy surface in hexagonal manganites is even flatter. While all members of the series have a frustrated in-plane antiferromagnetic (AFM) arrangement of the Mn^{3+} spin magnetic moments, the exact magnetic ground state varies with no obvious trend from compound to compound [9].

The goal of this work is to rationalize the evolution of the magnetic ground state across the hexagonal manganite series. We achieve this by decomposing the structural ground states into their distortions from

the high-symmetry prototype structure, and determining the effects of these distortions on the magnetic interactions. Our main finding is that the crystallographic K_1 mode, which consists of an in-plane triangular inwards or outwards breathing of the Mn and O ions, has a strong effect on the inter-planar exchanges and single-ion anisotropies, and ultimately determines the magnetic ground state of each material. Uncovering the details of this particular magneto-structural coupling sets the stage for engineering the magnetic order in this family of compounds.

II. STRUCTURE

The h - $RMnO_3$ structure consists of layers of corner-sharing MnO_5 trigonal bipyramids alternating in the c direction with triangular layers of R -site cations. All members of the series adopt the non-polar $P6_3/mmc$ space group at high temperature, and undergo a structural phase transition at a critical temperature T_c that ranges from 1200 – 1600 K, depending on the radius of the R site [10, 11]. At T_c the crystal symmetry lowers from non-polar $P6_3/mmc$ to polar $P6_3cm$, with the corresponding structural distortion consisting primarily of a K_3 mode, accompanied by a polar Γ_2^- mode [12], of the high-symmetry structure. An additional smaller structural distortion, corresponding to a K_1 mode, can

* tara.tosic@mat.ethz.ch

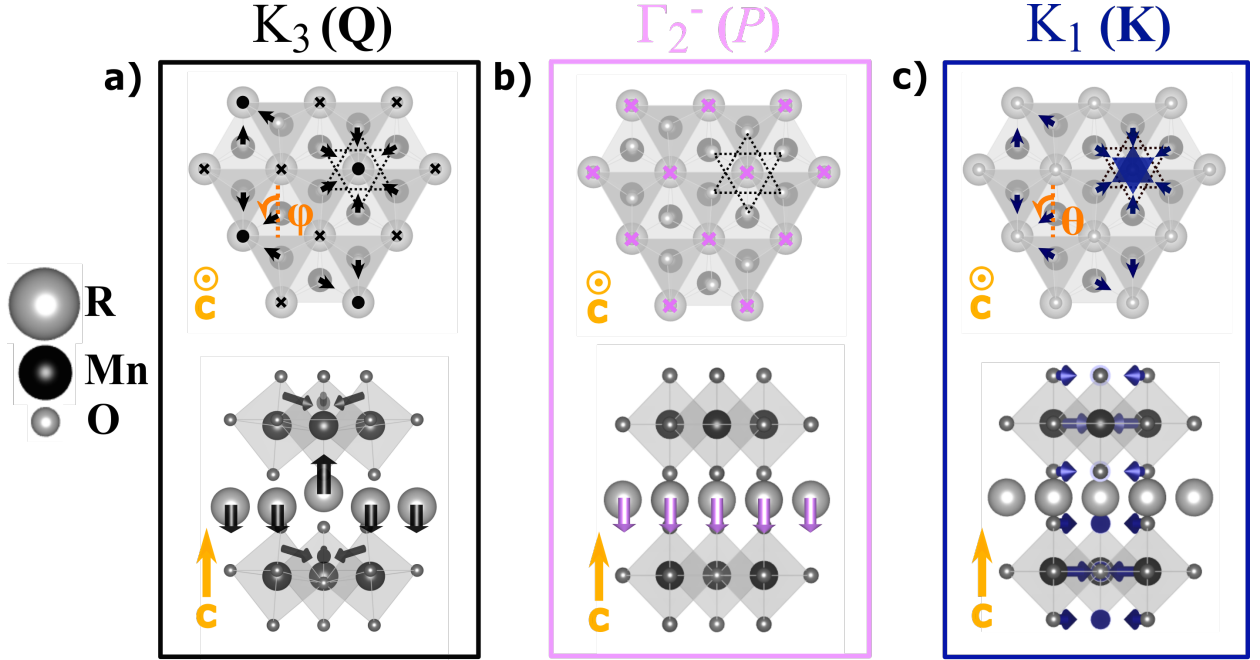


FIG. 1. Structural distortions associated with the coupled K_3 , Γ_2^- and K_1 modes and their respective order parameters \mathbf{Q} , \mathbf{P} and \mathbf{K} . **a)** $K_3(\mathbf{Q})$. Black arrows represent the buckling of the R ions as well as the direction of the bipyramidal tilts, the latter characterised by the angle ϕ (in this example, $\phi = 2\pi/3$). **b)** $\Gamma_2^-(\mathbf{P})$. Pink arrows show the vertical displacement of the R ions associated with a negative polarisation along the c axis. Note that displacements of O and Mn sites along c also occur within Γ_2^- but are not represented here. **c)** $K_1(\mathbf{K})$. Blue arrows indicate planar Mn and apical O displacements, their direction described by a characteristic angle θ (in the above example, $\theta = 2\pi/3$). Shaded blue triangles show stacked triangular Mn trimers breathing in, relative to the high symmetry position Mn trimers (shown in dotted black lines), as a result of a negative δx_{Mn} displacement.

also occur, and has been associated with the onset of magnetic ordering at lower temperature [13, 14]. We describe these distortion modes in detail next, reporting their contributions to both the experimentally observed structures and the Landau free energies which we extract using the INVARIANTS software from the group theoretical ISOTROPY Software Suite [15, 16].

A. K_3 and Γ_2^- modes

The primary order parameter driving the structural phase transition at T_c describes a zone boundary mode at $\mathbf{k} = (1/3, 1/3, 0)$, belonging to the K_3 irreducible representation of the high-symmetry $P6_3/mmc$ structure [1, 2, 4, 12]. The distortion, illustrated in Fig. 1a), consists of triangles of MnO_5 trigonal bipyramids tilting towards or away from their corner-shared O site, accompanied by a buckling of the R -ion plane along the c axis, and results in a trimerization of the lat-

tice. We write the associated primary order parameter as $\mathbf{Q} = Q(\cos(\phi), \sin(\phi))$, with Q giving the amplitude of the tilt and the angle ϕ its phase, as illustrated in Fig. 1a). The tilt angles have six-fold symmetry with $\phi = n\pi/3$ and the integer $n = 1, \dots, 6$. The ferroelectric polarisation \mathcal{P} results from a net displacement of the R ions along c belonging to the Γ_2^- irreducible representation of the $P6_3/mmc$ structure. \mathcal{P} emerges through a coupling to \mathbf{Q} , established to be of the form

$$f_{\mathbf{Q}\mathcal{P}} \propto Q^3 \mathcal{P} \cos(3\phi)$$

to lowest order in the Landau expansion of the free energy [1, 2, 12].

B. K_1 mode and its coupling to K_3 and Γ_2^-

In addition to the K_3 and the Γ_2^- modes, a third structural distortion is reported at temperatures below T_c , although with much smaller amplitude [14, 17–20];

group theoretical analysis of the minimum energy structure of YMnO₃, calculated using density functional theory (DFT), indicated that its corresponding ionic displacements are one and two orders of magnitude smaller than those of the Γ_2^- and K_3 modes, respectively [12]. The mode belongs to the K_1 irreducible representation of the $P6_3/mmc$ structure at the same $\mathbf{k} = (1/3, 1/3, 0)$ value as K_3 . K_1 involves collective planar displacements of the Mn ions and their apical O (O_{ap}) ions parallel to the directions of the bipyramidal tilts projected onto the ab plane, as depicted in Fig. 1c). Within this mode, the displacements of the O_{ap} ions are much smaller than those of the Mn ions [12]. Therefore, K_1 is discussed in terms of displacements δx_{Mn} of the Mn ions away from their high symmetry positions at their Wyckoff site $(1/3, 0, 0)$ [14]. Throughout this work, δx_{Mn} is expressed in units of fractional coordinates of the in-plane lattice parameters. Movements of Mn sites away ($\delta x_{Mn} > 0$) or towards ($\delta x_{Mn} < 0$) their corresponding trimerisation centres lead to a triangular breathing inwards and outwards of Mn sites that belong to the same trimer, as depicted by the respective contraction and expansion of blue coloured triangles in Fig. 1c).

The K_1 mode can also be described within the Landau free energy expansion by its order parameter $\mathbf{K} = \mathcal{K}(\cos(\theta); \sin(\theta))$, where θ describes the direction of the Mn and apical O displacements and \mathcal{K} is their amplitude. The K_1 mode is like the Γ_2^- mode in that it is stable in the high symmetry structure and it differs in that it is constrained by a three fold symmetry; i.e.

$$f_{\mathcal{K}} = \beta_1 \mathcal{K}^2 + \beta_2 \mathcal{K}^3 \cos(3\theta) \quad (1)$$

Since K_3 is the primary order parameter [12], the two coupling strengths β_1 and β_2 are positive and K_1 emerges through its couplings to the K_3 and Γ_2^- modes. These are third-order terms in the Landau free energy, with the form:

$$f_{\mathbf{KQP}} = \gamma_1 \mathcal{K} \mathcal{Q}^2 \cos(\theta + 2\phi) + \gamma_2 \mathcal{P} \mathcal{K} \mathcal{Q} \cos(\theta - \phi) \quad , \quad (2)$$

that is linear quadratic between K_1 and K_3 and trilinear between Γ_2^- , K_1 and K_3 . K_1 emerges improperly with $\gamma_{1,2} < 0$. Given the six possible values of ϕ

and that \mathcal{P} alternates sign between consecutive values of n [1], Eq. (2) is minimised for $\theta = \pi - 2\phi$ or $\theta = -2\phi$. Thus, the movement of the Mn and apical O sites within the K_1 mode is restricted along the direction defined by ϕ as illustrated in Fig. 1.

In Table I we list reported measured room-temperature and sub- T_N values of δx_{Mn} for six hexagonal manganites. The data illustrate three points. First, δx_{Mn} is small and therefore difficult to quantify, reflected in a spread of reported values. Second, there is no obvious trend in δx_{Mn} across the series. Finally, studies that measure Mn positions above and below T_N report trimers of Mn sites expanding below T_N for YbMnO₃ and YMnO₃ but contracting for ScMnO₃ and LuMnO₃, with no clear difference for HoMnO₃. Low temperature measurements have not been made for ErMnO₃. These observations lead to three open questions, which we address in this work: First, is δx_{Mn} non zero? Second, is there a trend in δx_{Mn} across the series? Third, what is the mechanism behind any activation of the K_1 mode, and is it temperature-dependent [19] or temperature-independent [14]?

III. MAGNETO-STRUCTURAL COUPLING

Having described the relevant structural distortions, we now turn to the magnetic properties and thus to the main objective of this study: the coupling between the magnetic order and the crystallographic structure.

A. Magnetic symmetry and properties

The small trigonal-bipyramidal crystal field splitting combined with exchange interaction favour the high-spin state on the formally d^4 , $L=0$ Mn³⁺ ions [5]. These Mn³⁺ magnetic moments order at a Néel temperature, $T_N \simeq 70 - 90$ K, with higher T_N values corresponding to smaller R -site radii [17, 24, 28]. The first nearest-neighbour interaction is strongly AFM and geometrically frustrated because of the triangular arrangement of the Mn ions [9].

There are four symmetry-allowed candidate magnetic irreducible representations (irreps), labelled $A_{1,2}$

	Sc	Lu	Yb	Er	Ho	Y
Radius [Å]	0.87	0.977	0.985	1.004	1.015	1.019
$T \geq T_N$	-0.0001(72) [‡] [21] 0.0008(85) [‡] [22]	-0.001 [‡] [19]	-0.0063(18) [‡] [22]	-0.020 [†] [23] -0.005 [†] [10]	-0.0072(12) [‡] [22] 0.002(8) [‡] [14]	-0.0155(4) [‡] [24] -0.0125(2) [‡] [21] -0.00861 [‡] [25] -0.0003(16) [‡] [19] 0.004(8) ^{‡*} [14]
$T \leq 10$ K	-0.0029(16) [‡] [22]	-0.003 [‡] [19]	-0.0023(19) [‡] [22]	(-)	-0.003(2) [‡] [14] 0.0025(86) [‡] [22]	0.0001(7) [†] [26] 0.0089 [‡] [19]

TABLE I. Diffraction measurements of δx_{Mn} displacements in the hexagonal manganites above (upper panel) and below (lower panel) the Néel temperature, T_N . The Shannon radii (for eight-coordinated 3+ states) are shown to indicate the radial trend [27]. [‡]Powder sample. [†]Single crystal sample. *Sample contained oxygen deficiency of 0.29(3) per formula unit. (-) No data available.

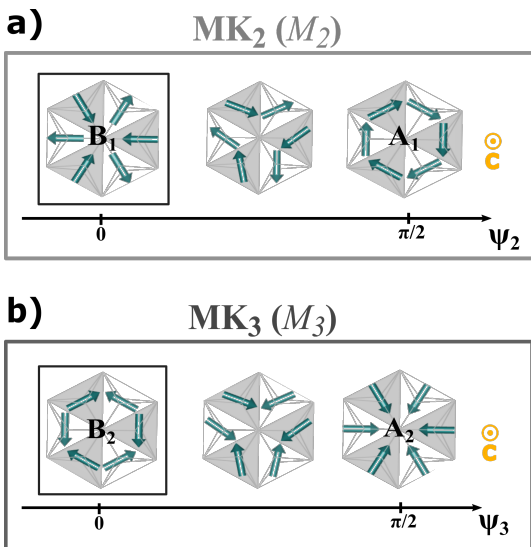


FIG. 2. Planar magnetic configurations associated with the two magnetic modes mK_2 and mK_3 , corresponding to order parameters \mathcal{M}_2 and \mathcal{M}_3 . The magnetic moments on each Mn site are represented by teal arrows. Consecutive planes are coloured in different shades. **a)** ψ_2 describes the evolution from B_1 ($\psi_2 = 0$) to A_1 ($\psi_2 = \frac{\pi}{2}$) via an out-of-phase rotation of spins belonging to two consecutive planes. **b)** ψ_3 describes the evolution from B_2 ($\psi_3 = 0$) to A_2 ($\psi_3 = \frac{\pi}{2}$) via an in-phase rotation of spins belonging to two consecutive planes.

and $B_{1,2}$, all of which have 120° first nearest-neighbour in-plane configurations. These irreps are generated under the zone boundary magnetic modes mK_2 or mK_3 described by the following respective order parameters: $\mathbf{M}_2 = \mathcal{M}_2 (\cos(\psi_2); \sin(\psi_2))$ and $\mathbf{M}_3 = \mathcal{M}_3 (\cos(\psi_3); \sin(\psi_3))$ as shown in Fig. 2 [13]. The

amplitudes $\mathcal{M}_{2,3}$ reflect the amount of correlation of magnetic moments on symmetry equivalent magnetic sites, and the angles $\psi_{2,3}$ describe the local direction of the Mn magnetic moments as sketched in Figs. 2a) and 2b). Within the four irreps, magnetic moments order either radially (A_2 and B_1) or tangentially (A_1 and B_2). The radial irreps A_2 and B_1 also allow for a weak out-of-plane ferromagnetic (FM) and AFM canting, respectively [5, 13]. Spins belonging to consecutive layers along the c axis can order with even (A) or odd (B) symmetry under the two-fold screw rotation $2\tilde{c}$ [1]. This results in two magnetic moments aligned along the same axis but belonging to consecutive planes pointing either parallel or anti-parallel to each other, corresponding respectively to a B- or A-type ordering. All the orders generated under mK_2 and mK_3 would have the same magnetic energy in the high symmetry structure. This energy degeneracy is broken as the structural symmetry is lowered to $P6_3cm$.

B. Coupling between K_3 and $mK_{2,3}$ modes

Magnetic order sets in on the low symmetry structure and this is expressed by a coupling between the primary order parameter and the magnetic order at fourth order in the Landau free energy expansion of the form [1, 5, 6, 29]

$$f_{\mathbf{Q}, \mathcal{M}_{2,3}} \propto \mathcal{M}_{2,3}^2 \mathcal{Q}^2 \cos^2(2\phi - 2\psi_{2,3}) \quad .$$

As a consequence of this coupling, there are two types of in-plane nearest-neighbour interactions: those between two Mn ions that share a trimerization center ($J_{\text{same trimer}}(st)$) (solid teal lines in Fig. 3), and those occupying neighbouring trimerization centers ($J_{\text{different trimer}}(dt)$) (solid black lines in Fig. 3). The low symmetry $P6_3cm$ structure also has two different inter-planar second nearest-neighbour exchanges, J_{1z} and J_{2z} . A total of six second nearest-neighbours interact with each given site i either via J_{1z} or J_{2z} , the former mediated by two equivalent (both grey in Fig. 3) R sites and the latter by two non-equivalent (one grey and one teal in Fig. 3) R sites. Finally, trigonal bipyramids have easy-plane single-ion anisotropy (SIA), with the hard axis tilted away from the c direction by the K_3 mode.

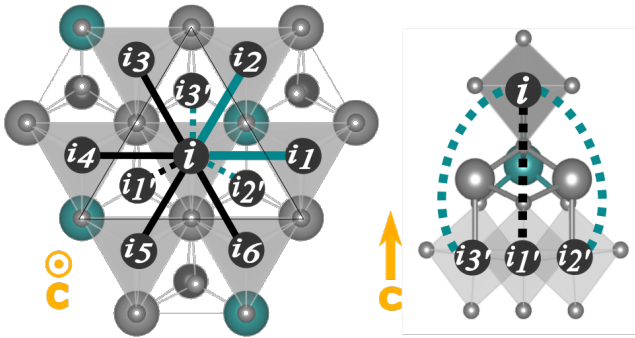


FIG. 3. Symmetric exchanges of a magnetic site i in the low symmetry $P6_3cm$ structure. Teal coloured R sites indicate trimerisation centres; nearest-neighbour sites i_1 and i_2 occupy the same trimer as site i , whereas sites i_3 , i_4 , i_5 and i_6 occupy different trimers. Solid teal and black lines represent same trimer (J_{st}) and different trimer (J_{dt}) nearest-neighbour exchanges, respectively. Dashed teal and black lines represent the inter-planar J_{1z} (with site $i_{1'}$) and J_{2z} (with sites $i_{2'}$ and $i_{3'}$).

Measurement of the exact magnetic ground state in the hexagonal manganites via scattering techniques is complicated by the issue of homometry [13]; magnetic symmetries obtained within one of the $mK_{i=1,2}$ modes lead to near equality of their magnetic structure factors in scattering data if $\delta x_{Mn} = 0$ [13, 20]. This is because the high symmetry position of the Mn sites (at Wyckoff position $(x \simeq \frac{1}{3}, 0, 0)$, corresponding to $\delta x_{Mn} \simeq 0$) lies in a mirror plane, $m_{\perp}[120]$ [14]. One way to address

this issue is by using polarised neutron scattering [26], since the polarised character of the incident beam allows the different ψ_2 and ψ_3 values to be distinguished, or second harmonic generation techniques [9] which are directly sensitive to the symmetry. B_1 and B_2 configurations (framed in black in Fig. 2) have been observed for different members of the series using optical second harmonic spectroscopy, with no evidence of A-type order [9].

C. Coupling between K_1 and $mK_{2,3}$ modes

Next, we review the experimental evidence for a sub- T_N δx_{Mn} structural distortion that motivates our investigation of a K_1 - $mK_{2,3}$ coupling [17, 19, 20]. In $YMnO_3$, powder diffraction measurements indicate that the experimental crystal volume deviates from the Einstein-Grüneisen volume predicted for a non-magnetic system [20, 30]. Additionally, resonant ultrasound spectroscopy detects an elastic stiffening in $YMnO_3$ as the crystal is cooled through T_N [17]. Both experimental techniques show that lattice strain scales with the square of the magnetic order parameter [17, 20]. The measured onset of this strain slightly above T_N [17] alludes to a magneto-structural coupling that coincides with the emergence of short range correlations between spins.

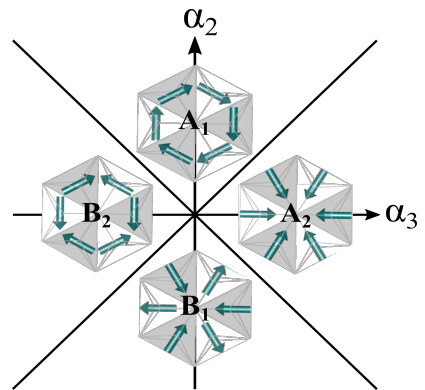


FIG. 4. Magnetic ground state in the phase space of the K_1 - $mK_{2,3}$ coupling parameters $\alpha_{2,3}$. Diagonal lines indicate $|\alpha_2| = |\alpha_3|$.

We will now motivate the K_1 - $mK_{2,3}$ coupling using symmetry arguments. The lowest order magneto-structural coupling term that appears in the Landau

Free Energy expansion and which remains invariant under the symmetry operations of the P6₃/mmc phase is at third order between the K₁ and the mK_{2,3} modes:

$$f_{\mathbf{K},\mathbf{M}_{2,3}} = \alpha_2 \mathcal{K} \mathcal{M}_2^2 \cos(\theta + 2\psi_2) + \alpha_3 \mathcal{K} \mathcal{M}_3^2 \cos(\theta + 2\psi_3) \quad , \quad (3)$$

where $\alpha_{2,3}$ are the coupling strengths. For a given K₁ displacement direction θ , these coupling terms are minimised for $i = 2, 3$, by solving:

$$\left. \frac{\partial f_{\mathbf{K},\mathbf{M}_{2,3}}}{\partial \psi_i} \right|_{\theta,\phi} = 0 \quad (4)$$

$$\Rightarrow -2\alpha_i \mathcal{K} \mathcal{M}_i^2 \sin(\theta + 2\psi_i) = 0 \quad .$$

Using Eq. (4), we calculate the ground-state magnetic phase diagram in the phase space of the two K₁-mK₂ and K₁-mK₃ coupling parameters (α_2 and α_3), shown in Fig. 4.

D. Model magnetic Hamiltonian

Next, in order to gain a microscopic understanding of the dependence of the magnetic ordering on the K₁ mode, we write down a model Hamiltonian, and calculate the interaction parameters as a function of the size and orientation of \mathbf{K} . We describe the energy of the magnetic moment on site i using the following Hamiltonian:

$$\mathcal{H}_i = \hat{e}_i \cdot \underbrace{\left(J_{st} \sum_{j=1,2} \hat{e}_{i_j} + J_{dt} \sum_{j=3,4,5,6} \hat{e}_{i_j} \right)}_{1^{\text{st}} \text{ nearest-neighbour exchange}} \quad (5)$$

$$+ \hat{e}_i \cdot 2 \underbrace{\left(J_{1z} \hat{e}_{i_1'} + J_{2z} \sum_{j'=2',3'} \hat{e}_{i_{j'}} \right)}_{2^{\text{nd}} \text{ nearest-neighbour exchange}} \quad (6)$$

$$+ \underbrace{A \cos(\psi_{2,3}^i)}_{\text{SIA}} \quad . \quad (7)$$

Here, $\hat{e}_i = (e_i^x, e_i^y, e_i^z)$ is the normalised magnetic moment of a site i where $i = 1, \dots, 6$ designates one of

the six magnetic sites of the unit cell and the indices i_j and $i_{j'}$ run over the first and second nearest-neighbours of site i , respectively, as sketched in Fig. 3. The nearest-neighbour couplings (mediated by the J_{st} and J_{dt} interactions) contribute equally to the energy in all four magnetic configurations, as can be seen by the 120° arrangement between nearest-neighbour sites in Fig. 2. The difference in energy between the A- and B-type configurations results from the inter-planar ordering and is described by the second term of \mathcal{H}_i : J_{1z} , where J_{2z} are the inter-planar exchanges illustrated in Fig. 2. The third term (7) gives the in-plane SIA, where A is defined as the energy difference between a spin pointing towards its trimerisation centre and perpendicular to it; $\psi_{2,3}^i$ is the angle describing the magnetic order within the two magnetic modes mK_{2,3} following the description in Figs. 2a) and 2b). Since the out-of-plane canting is known to be small we neglect any contribution to the total energy from rotation into the hard axis (see Methods section for further details).

Taking advantage of the fact that on a frustrated triangular lattice $\hat{e}_{i2'} + \hat{e}_{i3'} = -\hat{e}_{i1'}$, the interactions lifting the magnetic energy degeneracy between A₁, A₂, B₁ and B₂ can be reduced to an effective inter-planar exchange term $J_z = J_{1z} - J_{2z}$ and an effective in-plane anisotropy term A . Thus, we obtain the following single-spin Hamiltonian, reduced to only two relevant interactions, J_z and A , in which the first-nearest-neighbour AFM contributions have been absorbed into \mathcal{H}_0 :

$$\mathcal{H}_i = \hat{e}_i \cdot 2 \left[J_{1z} \hat{e}_{i1'} + J_{2z} \underbrace{(\hat{e}_{i2'} + \hat{e}_{i3'})}_{=-\hat{e}_{i1'}} \right] \quad (8)$$

$$+ A \cos(\psi_{2,3}^i) + \mathcal{H}_0$$

$$= 2J_z \hat{e}_i \cdot \hat{e}_{i1'} + A \cos(\psi_{2,3}^i) + \mathcal{H}_0 \quad . \quad (9)$$

Within this model, the energy, E_i , of each spin \hat{e}_i for each of the four allowed in-plane magnetic configurations is given by:

$$E_i(A_1) = -2J_z + \mathcal{H}_0 \quad , \quad (10)$$

$$E_i(A_2) = -2J_z + A + \mathcal{H}_0 \quad , \quad (11)$$

$$E_i(B_1) = 2J_z + A + \mathcal{H}_0 \quad \text{and} \quad (12)$$

$$E_i(B_2) = 2J_z + \mathcal{H}_0 \quad . \quad (13)$$

IV. METHODS

Total energies are obtained within DFT [31] based on the projector augmented-wave method [32] as implemented in the Vienna Ab initio Simulation Package (VASP 5.4.4) [33–36]. Calculations are performed using the Perdew-Burke-Ernzerhof (PBE) generalised gradient approximation [37, 38] combined with an on-site Coulomb repulsion of $U=4$ eV [5] and an exchange parameter of $J=1$ eV (following the Liechtenstein approach [39]) on the Mn sites [5, 40]. We use the Y_{sv} , Er_3, Lu, Mn and O VASP library pseudopotentials, with $4d$, $5p$, $5p$ and p electrons in the valence band, respectively. We compare the computed $E(B_2)$ - $E(B_1)$ energy difference with calculated values obtained via a different approximation, the local density density approximation, and find that the energy trend stays the same, albeit with an energy difference of $\simeq 0.2$ meV. The effects of the U and J values on the computed energies are also evaluated: there is no notable difference between $U=4$ and $U=6$ whilst $E(B_2)$ - $E(B_1)$ presents a steeper energy trend for $J=1$ than for $J=0$ with a maximal difference at big negative δx_{Mn} displacements of the order of 0.1 meV. The trends thus seem robust to our choice of U and J as well as our choice of pseudopotential. Finally, we use a cut-off of 700 eV and a gamma-centred k-point grid of $6 \times 6 \times 3$.

Geometries corresponding to the different values of the K_1 mode are obtained by selective dynamics relaxation of the cell, in which the Mn ions are fixed at positions away from their $K_1=0$ high symmetry position and the other atomic positions as well as lattice parameters are relaxed. Within selective dynamics, the $\frac{c}{a}$ ratio decreases quadratically and symmetrically around $\delta x_{\text{Mn}} = 0$ as Mn ions breathe inwards or outwards. This lattice ratio decreases by $\simeq 0.002$ for the computed compounds as Mn ions shift by $0.01 \times a$ from their high sym-

metry position. Note that, although K_1 is the only mode that allows a planar movement of Mn ions, the control of K_1 by a constraint on Mn positions within selective dynamics is not perfect. For example, the $\delta x_{\text{Mn}} = 0$ geometry still allows for very small displacements of O_{ap} within K_1 , and Γ_2^- and K_3 are activated, as they couple to K_1 , when the amplitude of \mathbf{K} is increased. However, the effect of these couplings is relatively small and will be the object of future works. For simplicity, we use the terms K_1 amplitude and δx_{Mn} interchangeably in this work. Important to note is that, even though Mn ions also relax to $\delta x_{\text{Mn}} \simeq 0$ in the fully relaxed geometries, the latter and the selective dynamics $\delta x_{\text{Mn}} = 0$ structures differ across the three compounds. The fully relaxed geometries have higher $\frac{c}{a}$ ratios, relative to their selective dynamics relaxed counterparts at $\delta x_{\text{Mn}} = 0$; namely 1.8788, 1.8654 and 1.8726 compared to 1.8900, 1.8654 and 1.8579 for LuMnO_3 , ErMnO_3 and YMnO_3 , respectively. Compared to the $\delta x_{\text{Mn}} = 0$ structure, the fully relaxed geometries have higher displacements corresponding Γ_1^+ and K_3 (by $\simeq 0.01$ and $\simeq 0.015$ Å respectively), as well as lower Γ_2^- displacements (by $\simeq 0.002$ Å). However, the K_1 mode amplitude is similarly small in both geometries. These structural differences are important to keep in mind when comparing the results for the fully relaxed and $\delta x_{\text{Mn}} = 0$ geometries.

A complete description of the SIA can be expressed through the τ_i matrix that is of the following form in each magnetic site's local coordinate system (defined for each Mn site with the local x axis pointing towards the trimerisation centre):

$$\tau_i = \begin{pmatrix} A_{xx} & 0 & A_{xz} \simeq 0 \\ 0 & A_{yy} & 0 \\ A_{xz} \simeq 0 & 0 & A_{zz} \end{pmatrix} \quad (14)$$

We find that the weak out-of-plane canting that is allowed in the A_2 and B_1 configurations [5] contributes negligibly to the total magnetic energy: the computed values border on the limit of the numerical precision of our DFT computations (10^{-5} eV). As a consequence, we do not include them in our model Hamiltonian.

Next, we describe how we compute the Hamiltonian parameters in Eq. (9). From Eqs. (18) and (19), we see

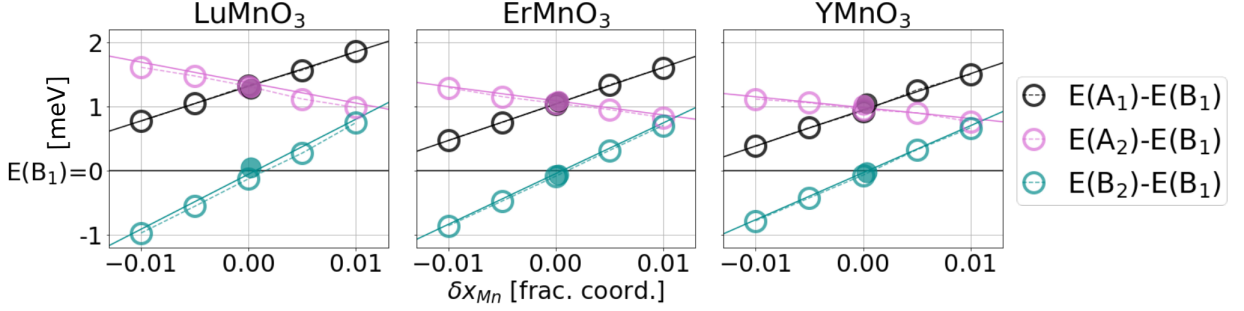


FIG. 5. Total energies of the planar magnetic configurations A_1 , A_2 and B_2 , relative to the energy of B_1 . Empty circles correspond to DFT calculated total energies for $\delta x_{\text{Mn}} \in [-0.01, 0.01]$ fractional coordinates and the dotted lines describe their energy trend. Full lines represent the model Hamiltonian calculated energies. Full circles are DFT total energies calculated on fully relaxed geometries.

that the J_z values can be obtained by subtracting the energy of configuration A_2 (A_1) from that of B_1 (B_2). We take the J_z value that is the average of the result from the two calculations (as shown in Eq. (17)):

$$J_z = \frac{1}{4}(E_i(B_1) - E_i(A_2)) \quad , \quad (15)$$

$$= \frac{1}{4}(E_i(B_2) - E_i(A_1)) \quad (16)$$

$$\Rightarrow J_z = \frac{(15) + (16)}{2} \quad . \quad (17)$$

Similarly, the A parameters are obtained by subtracting the energy of the A_1 (B_1) configuration from that of A_2 (B_2), and we take the average:

$$A = E_i(A_2) - E_i(A_1) \quad , \quad (18)$$

$$= E_i(B_2) - E_i(B_1) \quad (19)$$

$$\Rightarrow A = \frac{(18) + (19)}{2} \quad . \quad (20)$$

We then re-calculate A and J_z for a range of δx_{Mn} values and make a linear fit of their dependence on δx_{Mn} using a least squares method. The magnetic energies as a function of K_1 for different magnetic orders are obtained by substituting the A and J_z parameters into the Hamiltonian of Eq. (9). We verify the accuracy of our model and the extracted parameters by comparing our model magnetic energy trends following Eq. (9) with DFT calculated energies. The former are represented by solid lines in Fig. 5 and show excellent agreement with our total energy DFT calculations.

V. NUMERICAL RESULTS

We will focus on calculating the magnetic trends for the following three compounds, in order of increasing radius, $R = \text{Lu, Er and Y}$ for which the Shannon radii for the octahedrally coordinated 3+ ions are given in Table I. We begin by extracting the parameters A and J_z , defined in Eqs. (17) and (20) at K_1 amplitudes $\delta x_{\text{Mn}} = -0.01, -0.005, 0, 0.005$ and 0.01 which cover the spread of reported δx_{Mn} values (Table I).

A. Dependence of in-plane anisotropy on K_1 mode

Fig. 6a) shows the calculated total energy change as a function of in-plane spin angle on four different geometries: a fully relaxed structure and three selective dynamics geometries corresponding to $\delta x_{\text{Mn}} = -0.01, 0, 0.01$. Spins located in two consecutive planes are rotated in-phase, so that only the energy contribution of A is varied whilst keeping the J_z exchange energy constant. Note that this rotation is different to the ones spanning the $mK_{2,3}$ modes in Fig. 6, where both the in-plane anisotropy and inter-planar exchange energies change as a function of the rotation. We see that the angle dependence of the total energy E has opposite behaviour for $\delta x_{\text{Mn}} = -0.01$ and $+0.01$. E has its minimum value (-0.79 meV) for B_2 order ($\psi = n\frac{\pi}{2}$) in the $\delta x_{\text{Mn}} = -0.01$ geometry, whereas the B_1 order ($\psi = n\pi$) minimises E (at 0.69 meV) for $\delta x_{\text{Mn}} = +0.01$. This indicates that A , as defined by Eq. (19), has opposite values for opposite δx_{Mn} displacements and shows that

a linear combination of mK_1 and mK_2 magnetic symmetries is energetically unfavourable. A bigger in-plane anisotropy for $\delta x_{\text{Mn}} = -0.01$ than for $\delta x_{\text{Mn}} = +0.01$ can be attributed to a bigger K_1 mode displacement in the $\delta x_{\text{Mn}} = -0.01$ geometry (by $\simeq 0.0035 \text{ \AA}$). Interestingly, the energy surface flattens for $\delta x_{\text{Mn}} = 0$ but not completely as in the fully relaxed structure; the in-plane anisotropy has relatively small local minima at $\psi = n\frac{\pi}{2}$, like in the $\delta x_{\text{Mn}} = -0.01$ geometry. These local minima can again be attributed to the imperfect mapping between δx_{Mn} and \mathbf{K} mentioned in the Methods section.

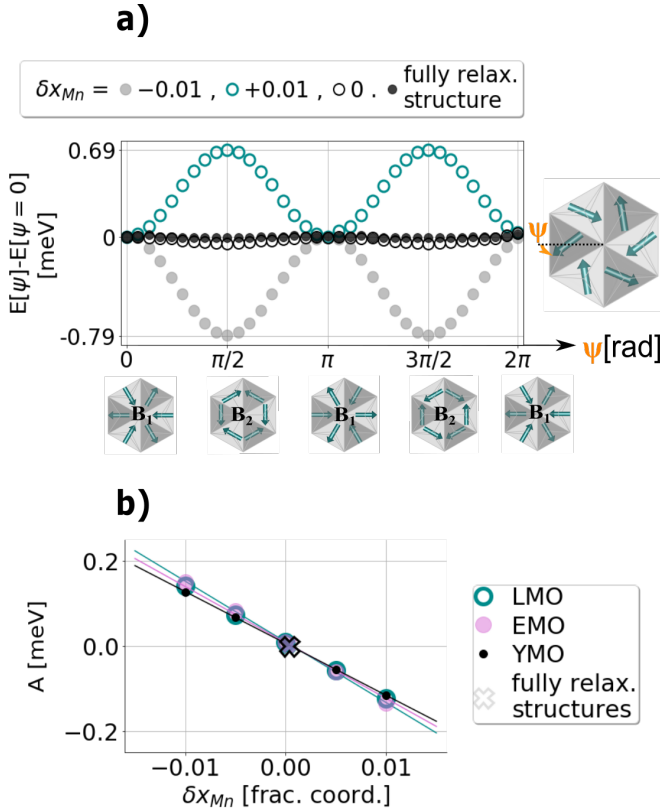


FIG. 6. SIA energy landscape as a function of δx_{Mn} . **a)** Total energy of YMnO_3 as a function of ψ for three different K_1 geometries ($\delta x_{\text{Mn}} = -0.01, +0.01$ and 0) and for a fully relaxed (fully relax.) structure. ψ describes the angle of an in-phase planar rotation of the \mathbf{B}_1 configuration. The in-plane anisotropy A is defined by the energy barrier at the local extrema. A is negative (positive) for $\delta x_{\text{Mn}} = -0.01$ ($+0.01$) and is almost non-existent for $\delta x_{\text{Mn}} = 0$. **b)** A calculated for $R = \text{Lu, Y}$ and Er for a range of δx_{Mn} geometries (circles) and for their fully relaxed geometries (crosses). The full lines represent a linear least squares fit of the DFT calculated energies.

We then calculate A following (20) for all three compounds, as shown in Fig. 6b). Importantly, we see

that the size of the single-ion anisotropy is similar in all three materials, and that the sign of A changes at approximately $K_1=0$ in each case. The sign change indicates a change in the preferred orientation of the spins within the easy plane.

B. Dependence of inter-planar exchange on K_1 mode

Next, we analyze the dependence of J_z on the K_1 mode and show the calculated behaviour in Fig. 7. Over the range of K_1 values studied, J_z is negative for all three materials. This corresponds to an FM (B-type) inter-planar interaction, with a linear dependence on K_1 consistent with the configurations observed in second harmonic generation measurements [9]. As the Mn ions shift away from their trimerisation centres, their apical oxygens shift by a smaller amount, leading to a decrease in the $\text{O}_{\text{ap}}\text{-Mn}$ orbital overlap and thus to a weaker inter-planar FM interaction. The displacement of the apical oxygens within the K_1 mode is similar across the three compounds, explaining the similarity in their $J_z[\mathbf{K}]$ gradient. Additionally, the effective inter-planar exchange is stronger for systems with smaller radius R cations and correspondingly bigger trimerisation, because J_z reflects the difference between the two different inter-planar exchanges. This difference, illustrated in Fig. 3, is larger for bigger bipyramidal tilts. Note that the inter-planar exchanges in the fully relaxed structures does not perfectly match the values for the $\delta_x\text{Mn} = 0$ geometry. The difference could be due to the slight differences of atomic positions between the two structures mentioned in the Methods section.

For comparison, we show as grey diamonds in Fig. 7 the J_z values extracted for hexagonal LuFeO_3 by Wang et al. in Ref. [40]. Hexagonal LuFeO_3 crystallises in the same structure as the hexagonal manganites and undergoes an analogous $\text{P6}_3/\text{mmc}$ to $\text{P6}_3\text{cm}$ structural phase transition. Its B-site chemistry differs from hexagonal manganites in that the Fe^{3+} ions are in a formally d^5 high-spin state. As a consequence of this extra electron, LuFeO_3 has a stronger inter-planar interaction [5] and magnetic order sets in at a relatively higher Néel temperature ($\simeq 150 \text{ K}$). The $J_z[\mathbf{K}]$ trend of LuFeO_3 in Ref. [40] is computed using the LDA+U method with U

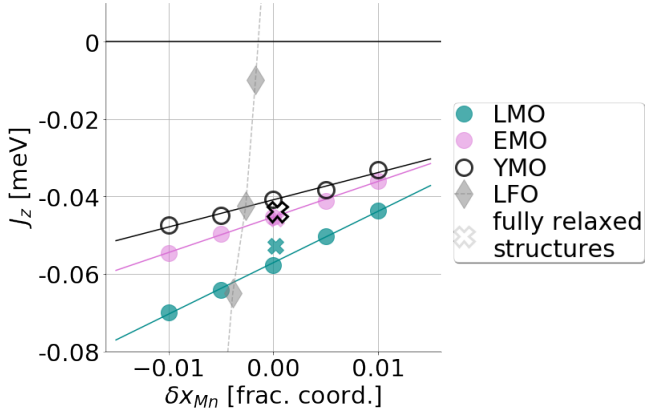


FIG. 7. Circles and crosses represent J_z values calculated in this work using Eq. (17) on $\delta x_{\text{Mn}} \in [-0.01, 0.01]$ and fully relaxed geometries, respectively. Grey diamonds connected by dotted lines show results for LuFeO_3 from Ref. [40].

= 4.5 eV and $J = 0.95$ eV. Note that our studies using different choices of functionals (see Methods sections) suggest that this difference in behaviour is not a result of small differences in the choice of computational parameters. Fig. 7 clearly indicates that the stronger J_z dependence on K_1 computed for LuFeO_3 [40] is necessary for small δx_{Mn} distortions to favour the A-type ordering observed in the hexagonal ferrites [5, 40].

C. R-site dependence

We note that the dependence of J_z and A on the size of the K_1 mode is sensitive to the R site, with LuMnO_3 showing the strongest variation and YMnO_3 the smallest. For $-0.015 < \delta x_{\text{Mn}} < +0.015$ the A and J_z parameters span $|A_{\text{max}} - A_{\text{min}}| = (0.43, 0.41, 0.39)$ and $|J_{z,\text{max}} - J_{z,\text{min}}| = (-0.04, -0.03, -0.02)$ for LuMnO_3 , ErMnO_3 and YMnO_3 respectively. This trend correlates with the size of the R -site radius, the smallest radius (Lu^{3+}) having the largest polyhedral tilts [7] and in turn the largest change of the magnetic interactions with K_1 . This effect is captured by the first term in the Landau free energy expression (2) in which the K_1 mode amplitude \mathcal{K} is linearly coupled to the square of the K_3 mode amplitude \mathcal{Q} , as well as by the coupling of \mathcal{K} to the squares of the two magnetic order parameters $\mathcal{M}_{1,2}$ in Eq. (3).

D. Ground state phase diagram

We summarise our calculated parameters and their effect on the magnetic ground state in the phase diagram of Fig. 8, where we plot the calculated A as a function of the calculated J_z over the interval $\delta x_{\text{Mn}} \in [-0.015, 0.015]$ for the three compounds. Since magnetic order is known unambiguously, this phase diagram allows us to predict the direction of the manganese displacement for which there is still a large spread in the experimental data. The fact that the B_1 state is measured in YMnO_3 and the B_2 state in ErMnO_3 implies opposite δx_{Mn} displacements in the two materials.

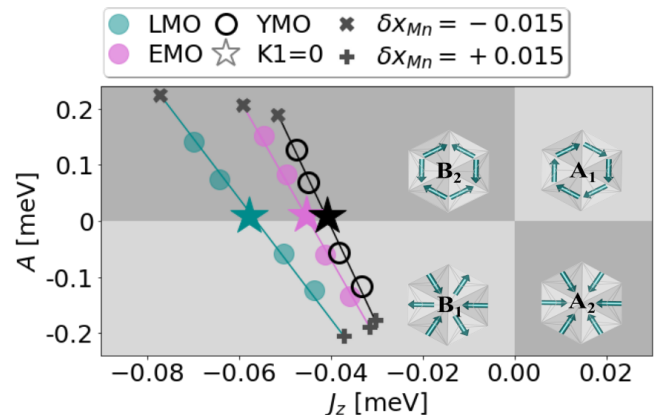


FIG. 8. Magnetic ground state phase diagram in the model Hamiltonian parameter phase space. Circles represent extracted (J_z, A) pairs and full lines are linear least-square fits plotted for the range $\delta x_{\text{Mn}} \in [-0.015, 0.015]$, going from top left to bottom right. Points marked by stars are the extracted values for $\delta x_{\text{Mn}} = 0$. Crosses and plus markers indicate parameters for $\delta x_{\text{Mn}} = -0.015$ and $+0.015$, respectively.

The phase diagram also sheds light on the origin of spin re-orientations observed in some hexagonal magnetites. Any change in the spin arrangement should correlate with the change in the Mn position as this creates transitions between A and B-type as well as between radial and tangential magnetic orders. For example, the B_2 to B_1 re-orientation in LuMnO_3 [9] as temperature decreases suggests a corresponding Mn displacement from negative to positive δx_{Mn} values. Interestingly, hexagonal LuFeO_3 has a sub- T_N spin re-orientation, similarly to LuMnO_3 , but from B_2 to A_2 as the temperature is lowered through 140 K [40]. This translates to not only a change in the sign of A (which is

Hamiltonian	Landau	Ground state
$A > 0$ $J_z < 0$	$ \alpha_3 > \alpha_2 $ $\alpha_3 < 0$	B₂ ($\psi_3 = n\pi$)
$A < 0$ $J_z < 0$	$ \alpha_2 > \alpha_3 $ $\alpha_2 < 0$	B₁ ($\psi_2 = n\pi$)
$A > 0$ $J_z > 0$	$ \alpha_2 > \alpha_3 $ $\alpha_2 > 0$	A₁ ($\psi_2 = n\frac{\pi}{2}$)
$A < 0$ $J_z > 0$	$ \alpha_3 > \alpha_2 $ $\alpha_3 > 0$	A₂ ($\psi_3 = n\frac{\pi}{2}$)

TABLE II. Mapping between Landau K_1 - $mK_{2,3}$ coupling parameters (α_2 and α_3), the model Hamiltonian parameters (J_z, A) and the magnetic ground state.

the case in LuMnO_3) but additionally, to a change in the sign of the inter-planar exchange interaction. This crossing from the left (B-type order) to the right (A-type order) part of our phase diagram is attributed to the steeper $J_z[\mathbf{K}]$ trend predicted for LuFeO_3 than for LuMnO_3 in Fig. 7.

Finally, in Table II we summarise the mapping between the A and J_z magnetic Hamiltonian parameters to the K_1 - $mK_{2,3}$ coupling parameters α_2 and α_3 and to the magnetic ground state. For example, a radial arrangement of spins combined with an AFM inter-planar order (**A₂**) corresponds to a ($A < 0, J_z > 0$) pair, which is equivalent to the following conditions on the K_1 - $mK_{2,3}$ coupling parameters: $|\alpha_3| > |\alpha_2|$ and $\alpha_3 > 0$. We have thus managed to describe the magnetic ground state of hexagonal Manganites in two different spaces: the phase space of the Landau free energy parameters (α_2, α_3) as well as of the magnetic Hamiltonian parameters (A, J_z).

VI. SUMMARY AND OUTLOOK

In summary, this work rationalizes the observed evolution of the magnetic ground state across the hexagonal manganite series, the reported sub T_N spin reorientations in LuMnO_3 , and explains why A-type magnetic configurations are energetically unfavourable [9].

To address the questions prompted by the experimental measurements of the Mn positions presented in Table I, we have determined, using symmetry arguments, the allowed coupling terms for $\delta x_{\text{Mn}} \neq 0$

by extending earlier expansions of the Landau free energy [1, 5, 12]. The extended Landau expansion reveals a non-linear coupling of the K_1 mode to the K_3 and Γ_2^- structural distortions, as well as to the magnetic order parameters. Furthermore, we have shown how $\delta x_{\text{Mn}} \neq 0$ changes the magnetic interactions, using a model magnetic Hamiltonian with DFT-computed parameters, singling out the easy-plane anisotropy and the inter-planar symmetric exchange terms as the relevant magnetic interactions that lift the magnetic energy degeneracy between the A_1, A_2, B_1 and B_2 orders. These two findings support experimental measurements of sub- T_N magnetoelasticity [17, 19, 20] and non-zero, temperature-dependent δx_{Mn} values, and suggest that the K_1 mode is responsible for both. In addition, our calculations indicate that, in materials with smaller R -site radii (and correspondingly larger K_3 distortions), the energy is more sensitive to changes in δx_{Mn} , motivating more precise experimental measurements of this quantity.

Our work indicates that the K_1 mode provides a gateway to controlling the magnetic order in the h - $RMnO_3$ series by varying its amplitude. We hope that this finding stimulates future studies investigating how the K_1 mode can be modified using external stimuli such as strain or doping.

ACKNOWLEDGEMENTS

This work was funded by the European Research Council (ERC) under the European Union's Horizon 2020 research and innovation program project HERO grant agreement No. 810451 and by the MARVEL national centre of competence in research (NCCR). Computational resources were provided by ETH Zürich and the Swiss National Supercomputing Centre, project IDs eth3 and s889.

-
- [1] S. Artyukhin, K. T. Delaney, N. A. Spaldin, and M. Maxim, Landau theory of topological defects in multiferroic hexagonal manganites, *Nat. Mater.* **13**, 42 (2013).
- [2] Q. Meier, M. Lilienblum, S. Griffin, K. Conder, E. Pomjakushina, Z. Yan, E. Bourret, D. Meier, F. Lichtenberg, E. Salje, N. Spaldin, M. Fiebig, and A. Cano, Global Formation of Topological Defects in the Multiferroic Hexagonal Manganites, *Phys. Rev. X* **7**, 041014 (2017).
- [3] S. H. Skjærvø, Q. N. Meier, M. Feyngenson, N. A. Spaldin, S. J. Billinge, E. S. Bozin, and S. M. Selbach, Unconventional Continuous Structural Disorder at the Order-Disorder Phase Transition in the Hexagonal Manganites, *Phys. Rev. X* **9**, 031001 (2019).
- [4] Q. N. Meier, A. Stucky, J. Teyssier, S. M. Griffin, D. van der Marel, and N. A. Spaldin, Manifestation of structural higgs and goldstone modes in the hexagonal manganites, *Phys. Rev. B* **102**, 014102 (2020).
- [5] H. Das, A. L. Wysocki, Y. Geng, W. Wu, and C. J. Fennie, Bulk magnetoelectricity in the hexagonal manganites and ferrites, *Nat. Commun.* **5**, 2998 (2014).
- [6] M. Giraldo, Q. N. Meier, A. Bortis, D. Nowak, N. A. Spaldin, M. Fiebig, M. C. Weber, and T. Lottermoser, Magnetoelectric coupling of domains, domain walls and vortices in a multiferroic with independent magnetic and electric order, *Nat. Commun.* **12**, 3093 (2021) (2021).
- [7] Y. Kumagai, A. A. Belik, M. Lilienblum, N. Leo, M. Fiebig, and N. A. Spaldin, Observation of persistent centrosymmetry in the hexagonal manganite family, *Phys. Rev. B* **85**, 174422 (2012).
- [8] F.-T. Huang, X. Wang, S. Griffin, Y. Kumagai, O. Gindele, M.-W. Chu, Y. Horibe, N. Spaldin, and S.-W. Cheong, Duality of Topological Defects in Hexagonal Manganites, *Phys. Rev. Lett.* **113**, 267602 (2014), publisher: American Physical Society.
- [9] M. Fiebig, D. Fröhlich, K. Kohn, S. Leute, T. Lottermoser, V. V. Pavlov, and R. V. Pisarev, Determination of the Magnetic Symmetry of Hexagonal Manganites by Second Harmonic Generation, *Phys. Rev. Lett.* **84**, 5620 (2000).
- [10] B. B. Van Aken, A. Meetsma, and T. T. M. Palstra, Hexagonal ErMnO_3 , *Acta Crystallogr. Section E* **57**, 38 (2001).
- [11] M. Bieringer and J. Greedan, Magnetic structure and spin reorientation transition in ScMnO_3 , *J. Solid State Chem.* **143**, 132 (1999).
- [12] C. J. Fennie and K. M. Rabe, Ferroelectric transition in YMnO_3 from first principles, *Phys. Rev. B* **72**, 100103 (2005).
- [13] C. J. Howard, B. J. Campbell, H. T. Stokes, M. A. Carpenter, and R. I. Thomson, Crystal and magnetic structures of hexagonal YMnO_3 , *Acta Crystallogr., Sect. B: Struct. Sci., Cryst. Eng. Mater.* **69**, 534 (2013).
- [14] T. Lonkai, D. Hohlwein, J. Ihringer, and W. Prandl, The magnetic structures of YMnO_3 and HoMnO_3 , *Appl. Phys. A: Mater. Sci. Process.* **74**, s843 (2002).
- [15] H. T. Stokes, D. M. Hatch, and B. J. Campbell, *Invariants, isotropy software suite*.
- [16] D. M. Hatch and H. T. Stokes, *INVARIANTS*: program for obtaining a list of invariant polynomials of the order-parameter components associated with irreducible representations of a space group, *J. Appl. Crystallogr.* **36**, 951 (2003).
- [17] R. I. Thomson, T. Chatterji, C. J. Howard, T. T. M. Palstra, and M. A. Carpenter, Elastic anomalies associated with structural and magnetic phase transitions in single crystal hexagonal YMnO_3 , *J. Condens. Matter Phys.* **26**, 045901 (2014).
- [18] J. Liu, C. Toulouse, P. Rovillain, M. Cazayous, Y. Gallais, M.-A. Measson, N. Lee, S. W. Cheong, and A. Sacuto, Lattice and spin excitations in multiferroic h-YbMnO_3 , *Phys. Rev. B* **86**, 184410 (2012).
- [19] S. Lee, A. Pirogov, M. Kang, K.-H. Jang, M. Yone-mura, T. Kamiyama, S.-W. Cheong, F. Gozzo, N. Shin, H. Kimura, Y. Noda, and J.-G. Park, Giant magneto-elastic coupling in multiferroic hexagonal manganites, *Nature* **451**, 805 (2008).
- [20] T. Chatterji, B. Ouladdiaf, P. F. Henry, and D. Bhattacharya, Magnetoelastic effects in multiferroic YMnO_3 , *J. Condens. Matter Phys.* **24**, 336003 (2012).
- [21] A. Muñoz, J. A. Alonso, M. J. Martínez-Lope, M. T. Casáis, J. L. Martínez, and M. T. Fernández-Díaz, Magnetic structure of hexagonal RMnO_3 ($\text{R}=\text{Y,Sc}$): Thermal evolution from neutron powder diffraction data, *Phys. Rev. B* **62**, 9498 (2000), publisher: American Physical Society.
- [22] X. Fabrèges, S. Petit, I. Mirebeau, S. Pailhès, L. Pinsard, A. Forget, M. T. Fernandez-Diaz, and F. Porcher, Spin-Lattice Coupling, Frustration, and Magnetic Order in Multiferroic RMnO_3 , *Phys. Rev. Lett.* **103**, 067204 (2009).

- [23] P. Liu, X.-L. Wang, Z.-X. Cheng, Y. Du, and H. Kimura, Structural, dielectric, antiferromagnetic, and thermal properties of the frustrated hexagonal $\text{Ho}_{1-x}\text{Er}_x\text{MnO}_3$ manganites, *Phys. Rev. B* **83**, 144404 (2011).
- [24] A. S. Gibbs, K. S. Knight, and P. Lightfoot, High-temperature phase transitions of hexagonal YMnO_3 , *Phys. Rev. B* **83**, 094111 (2011).
- [25] A. K. Singh, S. Patnaik, S. D. Kaushik, and V. Siruguri, Dominance of magnetoelastic coupling in multiferroic hexagonal YMnO_3 , *Phys. Rev. B* **81**, 184406 (2010), publisher: American Physical Society.
- [26] P. J. Brown and T. Chatterji, Neutron diffraction and polarimetric study of the magnetic and crystal structures of HoMnO_3 and YMnO_3 , *J. Condens. Matter Phys.* **18**, 10085 (2006).
- [27] R. D. Shannon, Revised effective ionic radii and systematic studies of interatomic distances in halides and chalcogenides, *Acta Crystallogr. Section A* **32**, 751 (1976).
- [28] B. Lorenz, Hexagonal Manganites—(RMnO_3): Class (I) Multiferroics with Strong Coupling of Magnetism and Ferroelectricity, *ISRN Condens. Matter Phys.* **2013**, e497073 (2013).
- [29] M. Fiebig, T. Lottermoser, D. Fröhlich, A. V. Goltsev, and R. V. Pisarev, Observation of coupled magnetic and electric domains, *Nature* (2002).
- [30] N. Sharma, A. Das, C. L. Prajapat, and S. S. Meena, Spin reorientation behavior in $\text{YMn}_{1-x}\text{M}_x\text{O}_3$ ($\text{M}=\text{Ti}$, Fe , Ga ; $x=0, 0.1$), *J. Magn. Magn.* **348**, 120 (2013).
- [31] V. I. Anisimov, F. Aryasetiawan, and A. I. Liechtenstein, First-principles calculations of the electronic structure and spectra of strongly correlated systems: the LDA+U method, *J. Phys. Condens. Matter* **9**, 767 (1997).
- [32] P. E. Blöchl, Projector augmented-wave method, *Phys. Rev. B* **50**, 17953 (1994).
- [33] G. Kresse and J. Hafner, Ab initio molecular dynamics for liquid metals, *Phys. Rev. B* **47**, 558 (1993).
- [34] G. Kresse and J. Hafner, Ab initio molecular-dynamics simulation of the liquid-metal–amorphous-semiconductor transition in germanium, *Phys. Rev. B* **49**, 14251 (1994).
- [35] G. Kresse and J. Furthmüller, Efficiency of ab-initio total energy calculations for metals and semiconductors using a plane-wave basis set, *Comput. Mater. Sci.* **6**, 15 (1996).
- [36] G. Kresse and J. Furthmüller, Efficient iterative schemes for ab initio total-energy calculations using a plane-wave basis set, *Phys. Rev. B* **54**, 11169 (1996).
- [37] J. P. Perdew, K. Burke, and M. Ernzerhof, Generalized Gradient Approximation Made Simple, *Phys. Rev. Lett.* **77**, 3865 (1996).
- [38] J. P. Perdew, K. Burke, and M. Ernzerhof, Generalized gradient approximation made simple, *Phys. Rev. Lett.* **77**, 3865 (1996).
- [39] A. I. Liechtenstein, V. I. Anisimov, and J. Zaanen, Density-functional theory and strong interactions: Orbital ordering in Mott-Hubbard insulators, *Phys. Rev. B* **52**, R5467 (1995).
- [40] H. Wang, I. V. Solovyev, W. Wang, X. Wang, P. J. Ryan, D. J. Keavney, J.-W. Kim, T. Z. Ward, L. Zhu, J. Shen, X. M. Cheng, L. He, X. Xu, and X. Wu, Structural and electronic origin of the magnetic structures in hexagonal LuFeO_3 , *Phys. Rev. B* **90**, 014436 (2014).
- [41] D. M. Ceperley and B. J. Alder, Ground State of the Electron Gas by a Stochastic Method, *Phys. Rev. Lett.* **45**, 566 (1980).
- [42] J. P. Perdew and A. Zunger, Self-interaction correction to density-functional approximations for many-electron systems, *Phys. Rev. B* **23**, 5048 (1981).
- [43] H. J. Xiang, E. J. Kan, S.-H. Wei, M.-H. Whangbo, and X. G. Gong, Predicting the spin-lattice order of frustrated systems from first principles, *Phys. Rev. B* **84**, 224429 (2011).

SUPPLEMENTARY INFORMATION

Effective J_z and A parameters extracted from total Energy calculations of the $A_{1,2}$ and $B_{1,2}$ magnetic configurations

	J_z	δx_{Mn}			A	δx_{Mn}		
		-0.01	0.0	0.01		0.01	0.0	0.01
LMO	(15)	-0.06(7)	-0.05(5)	-0.04(1)	(18)	0.14(0)	-0.00(2)	-0.14(6)
	(16)	-0.07(3)	-0.06(1)	-0.04(6)	(19)	0.16(3)	0.02(2)	-0.12(4)
EMO	(15)	-0.05(4)	-0.04(4)	-0.03(4)	(18)	0.13(7)	0.00(2)	-0.13(0)
	(16)	-0.05(6)	-0.04(7)	-0.03(7)	(19)	0.14(4)	0.01(5)	-0.11(7)
YMO	(15)	-0.04(6)	-0.04(0)	-0.03(2)	(18)	0.12(2)	0.00(4)	-0.12(3)
	(16)	-0.04(9)	-0.04(2)	-0.03(5)	(19)	0.13(1)	0.01(2)	-0.01(1)

TABLE III. Extracted Hamiltonian parameters (J_z , A) following Eq. (15) and Eq. (16) for Lu,Er,YMnO₃

The parameters used for the linear fit that ultimately produces Fig. 8 are the average of the two values obtained using equations Eq. (15) and Eq. (16) for $J_z[\delta x_{Mn}]$ and Eq. (18) and Eq. (19) for $A[\delta x_{Mn}]$ presented in table III.

Four-state method extracted parameters

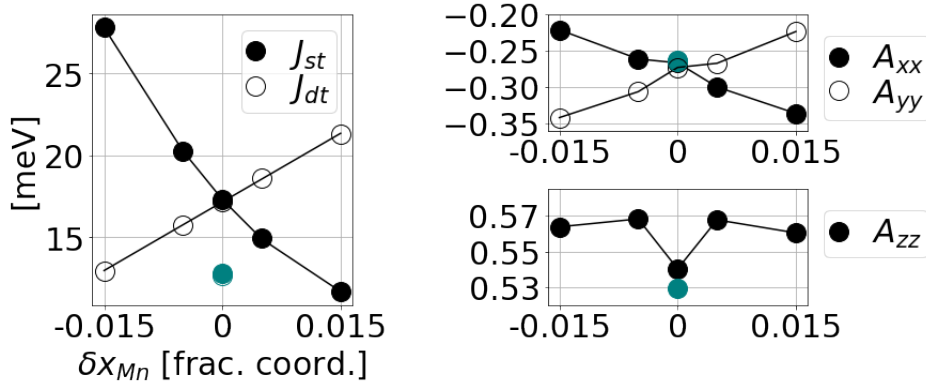


FIG. 9. Four-state method extracted symmetric exchanges for first nearest neighbours belonging to the same trimer (J_{st}) and different trimer (J_{dt}) vs K_1 for YMnO₃. Black symbols indicate parameters extracted for SD relaxed geometries, the corresponding parameters extracted on fully relaxed geometries are represented by the same symbols in teal. Energies (E) are calculated using the Ceperly and Alder local density approximation [41, 42], Y_{sv}, Mn_{sv} and O pseudopotentials and $U=4$ eV and $J=1$ eV.

Parameters were also extracted via the four-state method [43] for YMnO₃. As expected, the first nearest neighbour interactions, J_{st} and J_{dt} , are AFM and large, with values ranging from 10 - 30 meV, as shown in Fig. 9. Their strength is a direct function of the Mn-Mn distance. A negative (positive) value of δx_{Mn} corresponds to a contraction (expansion) of the triangle of Mn sites belonging to the same trimer which is reflected in the negative slope of J_{st} in Fig. 9. On the contrary, different trimer Mn sites are drawn farther apart (closer together) with negative (positive) δx_{Mn} ; this behaviour is illustrated by the upwards slope of J_{dt} in Fig. 9. SIA in-plane coefficients match the effective A values calculated via the method presented in the paper in Eq. (18) and Eq. (19).